

Rock organic carbon oxidation CO₂ release offsets silicate weathering sink

<https://doi.org/10.1038/s41586-023-06581-9>

Received: 28 February 2023

Accepted: 30 August 2023

Published online: 04 October 2023

Open access

 Check for updates

Jesse R. Zondervan^{1,4}✉, Robert G. Hilton¹✉, Mathieu Dellinger², Fiona J. Clubb³, Tobias Roylands³ & Mateja Ogrič³

Mountain uplift and erosion have regulated the balance of carbon between Earth's interior and atmosphere, where prior focus has been placed on the role of silicate mineral weathering in CO₂ drawdown and its contribution to the stability of Earth's climate in a habitable state^{1–5}. However, weathering can also release CO₂ as rock organic carbon (OC_{petro}) is oxidized at the near surface^{6,7}; this important geological CO₂ flux has remained poorly constrained^{3,8}. We use the trace element rhenium in combination with a spatial extrapolation model to quantify this flux across global river catchments^{3,9}. We find a CO₂ release of 68⁺¹⁸₋₆ megatons of carbon annually from weathering of OC_{petro} in near-surface rocks, rivalling or even exceeding the CO₂ drawdown by silicate weathering at the global scale¹⁰. Hotspots of CO₂ release are found in mountain ranges with high uplift rates exposing fine-grained sedimentary rock, such as the eastern Himalayas, the Rocky Mountains and the Andes. Our results demonstrate that OC_{petro} is far from inert and causes weathering in regions to be net sources or sinks of CO₂. This raises questions, not yet fully studied, as to how erosion and weathering drive the long-term carbon cycle and contribute to the fine balance of carbon fluxes between the atmosphere, biosphere and lithosphere^{2,11}.

The tectonic activity that builds mountains results in the uplift and exposure of organic carbon (OC) that has been incorporated in rocks (OC_{petro}) alongside silicate mineral phases. The OC_{petro} represents carbon stored in rocks that has accumulated over millions of years, previously sequestered from the atmosphere by photosynthesis and buried in sedimentary basins¹². Indeed, sedimentary and metasedimentary lithologies presently dominate the near-surface geology of the Earth, occupying about 64% of the Earth's surface¹³; these lithologies have OC_{petro} mass to mass concentration (denoted as [OC_{petro}]) ratios of about 0.25% to more than 1.0%, whereas igneous rocks have much lower values, effectively 0%, or in the case of some marine basalts, less than 0.1% (ref. 14).

Denudation supplies OC_{petro} to the surface through physical and chemical weathering^{3,15}; the rate varies with rock type, relief, tectonic uplift, climate and vegetation^{16,17}. Previous work has revealed OC_{petro} in soils and rivers^{6,18–20} and, using data from the solid load of rivers, quantified the erosion of unweathered OC_{petro}¹⁴ and its global flux at 43⁺⁶¹₋₂₅ MtC yr⁻¹ (refs. 14,19). However, for weathered OC_{petro}, estimated global rates of OC_{petro} oxidation and CO₂ release currently derive from carbon cycle mass balance arguments or ballpark upscaling of global river trace element fluxes⁸ and have a range of estimates from 38 MtC yr⁻¹ (ref. 21) to 100 MtC yr⁻¹ (ref. 22). The uncertainty of OC_{petro} oxidation fluxes is highlighted by recent work that cites a potential overall range for CO₂ release of 0–300 MtC yr⁻¹ (ref. 23).

To determine the role of rock weathering in the carbon cycle, we require a robust, global quantification of OC_{petro} oxidation over Earth's surface. Here, we combine (1) a compilation of OC_{petro} oxidation proxy

data from dissolved rhenium (Re) in well-studied catchments around the world, (2) new probabilistic models of global OC_{petro} stock and denudation and (3) a spatially explicit OC_{petro} oxidation model with quantified uncertainty. This approach derives a global flux by extrapolating proxy derived OC_{petro} oxidation data, while accounting for sampling bias across variables such as denudation rate and underlying geology.

Rhenium as an OC_{petro} oxidation proxy

The exploitation of the trace element Re as a proxy to study the oxidation of OC_{petro} across landscapes^{24,25} has been underpinned by (1) the link between OC accumulation in marine sediments and organic matter being a host of Re (refs. 26,27); (2) the paired loss of Re and OC_{petro} during weathering of sedimentary rocks^{7,25,28}; and (3) the geochemical behaviour of Re being exported as a dissolved oxyanion²⁹, flushed from a near-surface, oxidative weathering zone²⁵. Studies tracking the fate of carbon released from the lithosphere during OC_{petro} weathering have found it can directly enter the atmosphere as CO₂ (refs. 30,31) or first dissolve as inorganic carbon in water³², and some can be incorporated into microbial biomass⁸.

In this study, we compile published estimates of OC_{petro} oxidation using the dissolved Re proxy, supplemented with new estimates derived from published dissolved Re concentrations^{7,9,24,33} (Methods). A forward-mixing model is used to quantify the proportion of dissolved Re from OC_{petro} oxidation using ion ratios^{24,34}, while constraints on the OC_{petro} to Re ratio ([OC_{petro}]/[Re]) in weathered rocks come from new and

¹Department of Earth Sciences, University of Oxford, Oxford, UK. ²EDYTEM-CNRS-University Savoie Mont Blanc (USMB), Chambéry, France. ³Department of Geography, Durham University, Durham, UK. ⁴Present address: Department of Earth Sciences, University College London, London, UK. ✉e-mail: j.zondervan@ucl.ac.uk; robert.hilton@earth.ox.ac.uk

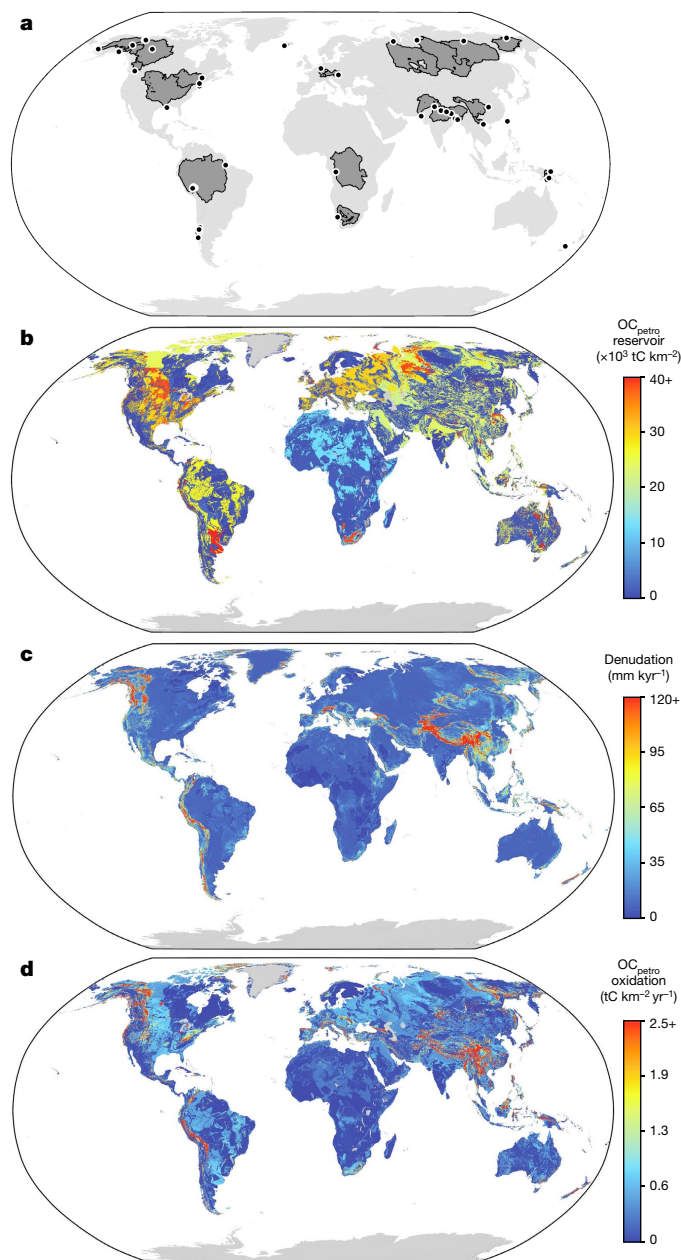


Fig. 1 | Spatial patterns of global OC_{petro} stock and oxidation. **a**, Locations of Re proxy samples and their upstream catchments. **b**, Spatially explicit estimates of OC_{petro} stocks in the upper 1 m of bedrock. **c**, Spatial model of rock denudation derived from ^{10}Be data and a global raster of topographic slope. **d**, OC_{petro} oxidation fluxes extrapolated by our calibrated spatial model over the global surface.

published measurements (Methods and Supplementary Table 3). Our compilation comprises 59 river basins, covering a range of drainage areas (50–5,900,000 km²), denudation rates and climate regimes (Fig. 1), excluding river basins with high Re pollution levels such as the Danube, Yangtze and Mississippi⁹ (Methods). The total OC_{petro} weathering flux constrained from the Re proxy across the drainage area of river basins in the dataset is 18 MtC yr⁻¹ (17–23 MtC yr⁻¹ within one standard deviation). The river basins in this study cover 18% of the Earth’s continental surface, and this flux would thus scale to 98⁺²⁸ MtC yr⁻¹ globally. However, OC_{petro} stocks are spatially heterogeneous, which may affect this scaling. In the next section, we obtain a robust representative total OC_{petro} weathering flux using a spatial extrapolation model that considers patterns in OC_{petro} stock and denudation rates.

Distribution of OC_{petro} availability

We spatially quantify the carbon stock and weathering flux of OC_{petro} at Earth’s surface using a data-driven modelling approach. Our model incorporates topographic and lithological factors to estimate OC_{petro} stocks, denudation rates and oxidative weathering rates, and is calibrated using our Re-proxy compilation (Supplementary Table 1). Unlike silicate weathering, which quickly becomes kinetically limited with increasing mineral supply by denudation³⁵, OC_{petro} weathering appears to be predominately a supply-limited process⁸. This is reflected in oxidation rates which scale with erosion up to some of the highest erosion rates found on Earth, such as Taiwan and the European Alps^{7,25}. Recent work at the rock outcrop scale has shown that temperature and hydrology can control OC_{petro} oxidation and CO₂ release over time in locations with very high rates of denudation^{30,31}. However, though the spatial control of denudation rates is well demonstrated on intercatchment OC_{petro} oxidation rates^{7,25} our spatial catchment-scale Re-proxy compilation does not express other environmental controls (Methods). While temperature and hydrology controls likely operate, based on the available data, their spatial predictive power is small. Here, oxidative weathering is modelled at a 1-km² grid scale, resolving at the scale of catchments constrained by the Re proxy (Supplementary Table 1).

The flux of CO₂ release by OC_{petro} oxidation, J_{ox} (mass × length⁻² × time⁻¹), can be expressed by a mass balance of the form:

$$J_{\text{ox}} = \varepsilon \times \rho \times [OC_{\text{petro}}] \times \chi \tag{1}$$

where ε (length × time⁻¹) is the denudation rate, ρ is rock density (mass × length⁻³), $[OC_{\text{petro}}]$ is the OC concentration in rock (mass × mass⁻¹) and χ is the weathering intensity as the fraction of OC_{petro} weathered from rock. Weathering intensity χ has been shown to vary between low values of 0.2 in highly erosive settings⁷ and very high values of 0.98 in slow denudation settings⁸ with most falling in a range of 0.6–0.9 (refs. 7,33,34). Thus, χ presents a substantially smaller variance across environments in contrast to denudation rate and $[OC_{\text{petro}}]$, which vary spatially by more than four orders of magnitude.

To constrain the stock of OC_{petro} in the near surface, we use $[OC_{\text{petro}}]$ from the US Geological Survey rock geochemical database, combined with global lithological maps¹³ and spatial chemical lithology classifications³⁶. Our geospatial model simulates a large global near-surface OC_{petro} stock, with the estimate and its interquartile range at 1490⁺²⁵⁸⁰₋₉₈₀ Gt OC_{petro} in the first metre of bedrock. This estimate is consistent with a global estimate of 1,100 Gt OC_{petro} within the first metre of sedimentary rocks¹⁴, a reassessment of deep soil radiocarbon data which provides evidence for OC_{petro} inputs²⁰, and is of comparable magnitude to that of global soils (2,060 ± 215 Gt OC)³⁷ and marine sediments (2,322 ± 75 Gt OC)³⁸. As opposed to soil OC stocks, the distribution of OC_{petro} is primarily controlled by the geological history of continents. While the highest $[OC_{\text{petro}}]$ is found in black shales (Extended Data Fig. 4), such rocks compose a tiny fraction of the Earth’s surface¹³, and instead, most OC_{petro} is found in fine-grained sedimentary deposits such as shales (Fig. 1b). Geospatial patterns reveal low OC_{petro} stocks on the African continent (Fig. 1b), owing to a low occurrence of fine-grained sedimentary rocks. In contrast, substantial portions of Eurasia, South America and the middle of North America east of the Rocky Mountains contain shales. The overlap of OC_{petro} stocks and patterns of denudation, driven mostly by rock uplift in mountains, determines the exposure of this OC stock to oxidative weathering. We estimated denudation using a probabilistic spatial model that incorporates catchment-scale cosmogenic radionuclide (CRN) denudation rates³⁹, digital topography⁴⁰ and lithological maps¹³. The resultant modelled global denudation rate and its interquartile range is 11⁺¹³₋₆ Gt yr⁻¹, within range of recent estimates of global denudation at 28⁺⁶⁴₋₂₀ Gt yr⁻¹ (ref. 16) and 15 ± 2.8 Gt yr⁻¹ (ref. 17).

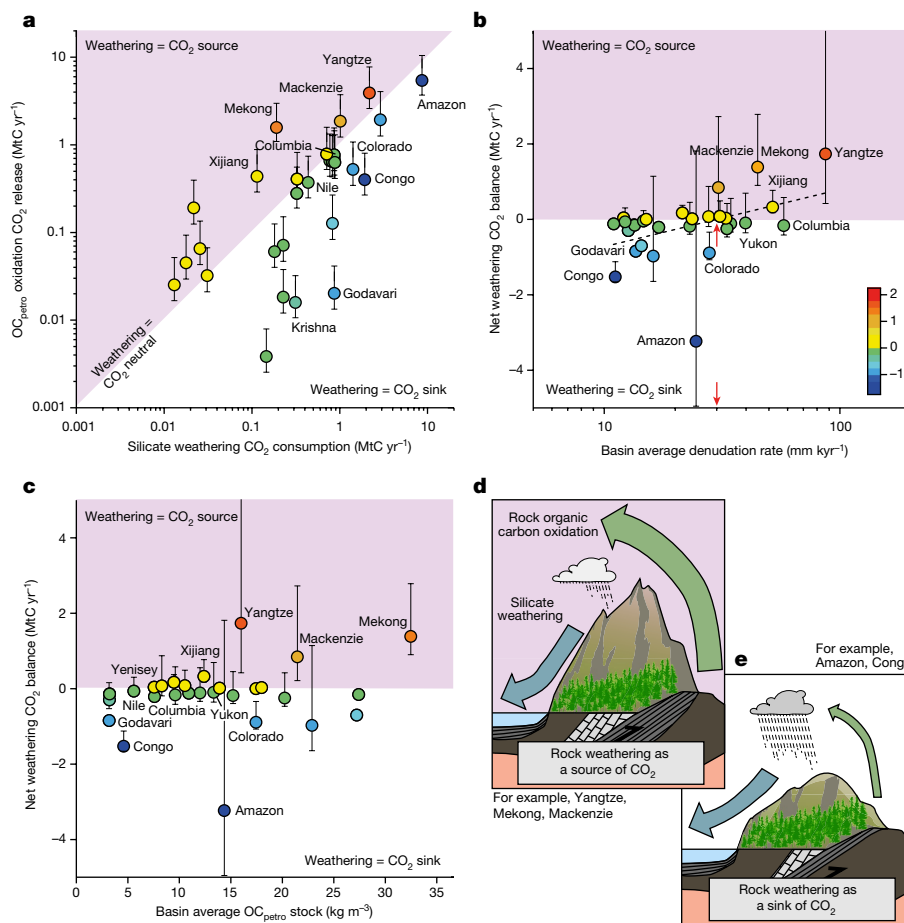


Fig. 2 | Earth's major river basins, their silicate weathering carbon sinks and OC_{petro} weathering carbon sources, and their overall rock weathering budget based on these fluxes. a, Silicate¹⁰ versus OC_{petro} weathering fluxes and their net values. Basins that produce a net source of CO_2 are shown in the shaded half of the plot, with the net magnitude of the weathering CO_2 flux illustrated by the symbol colour (in $MtC\ yr^{-1}$). **b, c**, Net weathering balance versus basin-average denudation (red arrow: cross-over at about $30\ mm\ kyr^{-1}$)

Spatial model of OC_{petro} oxidation

Rather than the more classical mean-field parametrization schemes previously employed to model OC_{petro} supply rates¹⁴, we use a probabilistic approach⁴¹ that accounts for the uncertainties in both variables in a spatial model. In each cell, empirical probability distributions of $[OC_{\text{petro}}]$ based on rock type (Extended Data Fig. 4) and probability distributions of denudation based on rock type and topographic slope (Extended Data Fig. 6) are sampled in 10,000 Monte Carlo simulations. We calibrated the geospatial model by minimizing the residuals between the modelled cell values of OC_{petro} oxidation rates (J_{ox}) and our compilation of Re-proxy data at the river catchment scale (Methods). Thus, our approach describes the spatial patterns of oxidative weathering rate as a function of topographic slope and rock type, which leads to simulations that are consistent with an assessment of global rock nitrogen weathering patterns which are dominated by denudation of fine-grained sedimentary rocks⁴¹.

Using our spatial model, we estimate that oxidative weathering of OC_{petro} releases $68^{+18}_{-6}\ MtC\ yr^{-1}$ as CO_2 from the land-surface environment. The flux is lower than our spatially uncorrected extrapolation of Re-proxy measurements ($98^{+28}_{-9}\ MtC\ yr^{-1}$), consistent with the slight bias towards high denudation rate settings in the river basin dataset. The best estimate of the oxidative weathering flux is higher than an independent estimate of OC_{petro} erosion and river transport (that is,

(b) and versus basin-average OC_{petro} stock (c). Error bars represent uncertainty of OC_{petro} oxidation model outputs based on the uncertainty of the training data (see Methods, ' OC_{petro} oxidation yields and uncertainties'). **d, e**, Variable rates of uplift and erosion, climate and OC_{petro} stocks across Earth's surface impact OC_{petro} and silicate weathering rates differently, leading to regions where rock weathering is a source (d) or a sink (e) of CO_2 .

the export of OC_{petro} that has not been weathered) of $43^{+61}_{-25}\ MtC\ yr^{-1}$ based on river solid load composition and flux¹⁹, even though the uncertainties overlap. While a direct comparison of these estimates is difficult based on their quantification from dissolved versus particulate river chemistry and flux, they suggest an average weathering intensity of OC_{petro} of about 60%, which is consistent with studies from large river basins¹⁹ and intensities measured in soils^{8,42}.

The OC_{petro} oxidation model can estimate the turnover time of OC_{petro} at the surface. When combined with OC_{petro} stocks, the model suggests that $0.05^{+0.12}_{-0.03}\ yr^{-1}$ of the global OC_{petro} stock in the first 10 cm of bedrock may be oxidized during denudation and weathering. A global OC_{petro} loss rate of about $0.05\ yr^{-1}$ equates to a carbon turnover time (the ratio of total OC_{petro} to carbon outputs by oxidation) of approximately 2,000 years. This is about double the corresponding value for global soils⁴³, but shorter than turnover times in tundras of approximately 3,900 years⁴⁴. Given the large stock of OC_{petro} that we report (approximately $150\ Pg\ C$ in the upper 10 cm) and its turnover time, OC_{petro} cannot be assumed to be inert and passive in the shallow subsurface. The input of OC_{petro} into soils can also impact soil residence time estimations and lead to an underestimation of soil carbon exchange fluxes with the atmosphere²⁰.

Across the land surface, OC_{petro} weathering is relatively focused (Fig. 1d), with variations in rock type and relief, which drive OC_{petro} content and denudation, respectively, determining the magnitude

Article

of OC_{petro} oxidation and CO_2 release. Large regions of the African continent have lower OC stocks in bedrock and have lower relief, which together limit OC weathering. In contrast, higher OC_{petro} oxidation rates are estimated for northern latitudes, where OC -rich rock and high-relief landscapes are more prevalent. Overall, 10% of the Earth surface with the highest OC_{petro} oxidation rates account for 60% of the global flux in our model. The world average rate is $0.5 \text{ tC km}^{-2} \text{ yr}^{-1}$, hotspots (surpassing ten times world average) and hyperactive areas (all areas surpassing five times world average) are responsible for 32% and 44% of CO_2 emissions, respectively, while representing only 1.2% and 3% of ice-free terrestrial land area, respectively. OC_{petro} weathering rates in our model are more spatially concentrated than a 1-km resolution spatial model of silicate weathering⁴⁵, where hotspots (0.51% by area) and hyperactive areas (2.9% by area) accounted for 8.6% and 19.6% of total CO_2 consumption, respectively. This outcome appears reasonable because OC_{petro} is less common spatially than silicate minerals and reacts faster^{3,25}.

Weathering CO_2 sources versus sinks

The OC_{petro} weathering flux and release of CO_2 to the atmosphere of $68^{+19}_{-6} \text{ MtC yr}^{-1}$ is similar to global terrestrial CO_2 uptake by silicate weathering ($94\text{--}143 \text{ MtC yr}^{-1}$)¹⁰. Silicate weathering involves dissolved and gaseous CO_2 uptake through bicarbonate production and the release of dissolved ions, some of which then precipitate as marine carbonate rocks⁴. The resultant total transfer of carbon from the atmosphere to the lithosphere by silicate weathering is $47\text{--}72 \text{ MtC yr}^{-1}$. Besides their opposing impacts on the transfer of carbon between the atmosphere and lithosphere, fluxes of silicate weathering versus OC_{petro} oxidation may have contrasting responses to climate. Silicate weathering is invoked as negative feedback to climate warming through increased rates of silicate weathering from increased temperature and a more vigorous hydrological cycle, drawing down more CO_2 (refs. 35,46). In contrast, in high denudation rate settings the CO_2 release from OC_{petro} oxidation may increase with temperature^{30,31}, while links to glacial erosion processes complicate the feedback between oxidative weathering and climate³³.

Silicate and OC_{petro} weathering processes may overlap, as sedimentary rocks contain silicate minerals as well as OC_{petro} ; however, the relative magnitude of these fluxes will vary spatially with climate, rock type and denudation^{35,46}. We assess the net balance of rock weathering within major river basins (Fig. 2), using our OC_{petro} oxidation model and silicate weathering estimates¹⁰.

Within uncertainties, rock weathering in about a third of the major river basins is a net source of CO_2 after OC_{petro} oxidation is considered, even while using the values of initial atmospheric CO_2 consumption of silicate weathering rather than the smaller quantity of CO_2 eventually locked up in the lithosphere through carbonate precipitation of the associated released dissolved ions (Fig. 2a). The Yangtze (Changjiang) and Mekong draining the eastern flanks of the Himalayas and the Mackenzie River draining shales west of the Rockies in Canada are major sources of CO_2 from rock weathering. These high-emitting basins have in common some of the highest basin-average denudation rates and OC_{petro} stocks (Fig. 2b,c), which is consistent with OC_{petro} oxidation being driven by OC_{petro} stocks and denudation (equation (1))^{7,8,25}.

Hotspots of CO_2 release during rock weathering appear to lie at the edges of major active mountain ranges where relatively young, marine sedimentary deposits are uplifted and supplied to the oxidation process through denudation. Examples include the shales of the Himalayan collision zones and east of the Rocky Mountains (Fig. 1b,d). On the other hand, basins where rock weathering is the biggest net sink of CO_2 do not necessarily lie at the extremes of low denudation and low OC_{petro} stocks. Though the tropical Congo River and volcanics-dominated Godavari River basins have low basin-average denudation rates and low OC_{petro} stocks, neither one is the biggest weathering sink; that

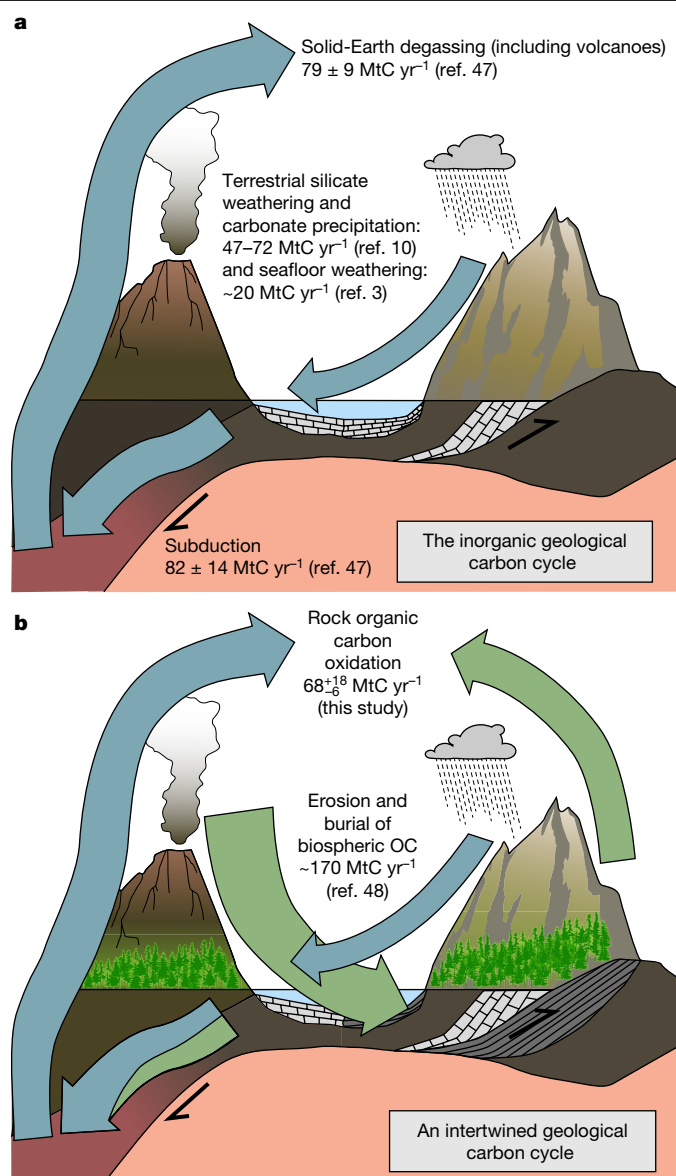


Fig. 3 | A shift in understanding the geological carbon cycle. a, The inorganic geological carbon cycle relies on a global balance between solid-Earth CO_2 degassing and silicate weathering. **b**, The emerging understanding of the role of organic carbon in the global geological carbon cycle, supported by the high flux of OC_{petro} oxidation reported in this study. Hence, the biological, chemical and physical processes of biospheric OC production, burial and release control long-term climate variability and stability.

distinction applies to the Amazon River basin, which lies in the global middle range of denudation rates and OC_{petro} stocks (Fig. 2b,c). There, the kinetically limited silicate weathering reaction benefits from long sediment residence times and a warm, humid climate.

While the Andes is a hotspot for OC_{petro} oxidation fluxes (Fig. 1d), the exceptionally large lowland drainage area of the Amazon means that OC_{petro} oxidation may be supply limited. In a third of river basins weathering remains carbon neutral within uncertainty; for example, such is the case with the volcanic-rich Columbia River catchment.

To avoid large swings in atmospheric CO_2 over millions of years and maintain an apparent close balance of CO_2 sources and sinks^{2,11}, any potential imbalances in weathering-derived carbon fluxes must be addressed by accounting for other components in the long-term carbon cycle. Solid-Earth degassing associated with volcanoes and diffuse release from metamorphism in subduction zones is responsible for

79 ± 9 MtC yr⁻¹ released into the atmosphere (Fig. 3a)⁴⁷, while any additional (non-subduction) global CO₂ release during orogenic metamorphism and sulfide oxidation and inorganic C uptake during seafloor weathering are more poorly constrained³. As our results show that the weathering of OC_{petro} offsets silicate weathering in the long-term carbon cycle, a large additional sink of CO₂ is needed. This may be provided by burial of organic matter in ocean sediments, which could contribute as much as 170 MtC yr⁻¹ (Fig. 3b)⁴⁸. In addition, as OC_{petro} fluxes can overtake silicate weathering during periods of more intense uplift and erosion (Fig. 2b,d and Extended Data Fig. 8), the question whether orogenic periods in Earth history are sources or sinks of atmospheric CO₂ is now a reopened question^{3,31,49,50}. The net balance will depend on factors such as transport of terrestrial biospheric carbon to oceans (157⁺⁷⁴₋₅₀ MtC yr⁻¹) and its burial¹⁹. A global comparison of catchment-scale OC_{petro} oxidation yields and estimated terrestrial biospheric OC burial (Extended Data Fig. 8) suggest the OC burial can apparently offset or even overcompensate CO₂ release from OC_{petro} oxidation. This understanding persists when the additional marine OC burial sink in sediment is factored into global flux estimates (Fig. 3b)⁴⁸. The dynamics of Earth's weathering thermostat thus need to be revisited to account for variation in all these fluxes and consider how their relative importance may have changed as life evolved and the OC stocks of sedimentary rocks have increased^{13,22}.

Online content

Any methods, additional references, Nature Portfolio reporting summaries, source data, extended data, supplementary information, acknowledgements, peer review information; details of author contributions and competing interests; and statements of data and code availability are available at <https://doi.org/10.1038/s41586-023-06581-9>.

- Chamberlin, T. C. An attempt to frame a working hypothesis of the cause of glacial periods on an atmospheric basis. *J. Geol.* **7**, 545–584 (1899).
- Berner, R. A. & Caldeira, K. The need for mass balance and feedback in the geochemical carbon cycle. *Geology* **25**, 955–956 (1997).
- Hilton, R. G. & West, A. J. Mountains, erosion and the carbon cycle. *Nat. Rev. Earth & Environ.* **1**, 284–299 (2020).
- Gaillardet, J., Dupré, B., Louvat, P. & Allègre, C. J. Global silicate weathering and CO₂ consumption rates deduced from the chemistry of large rivers. *Chem. Geol.* **159**, 3–30 (1999).
- Raymo, M. E. & Ruddiman, W. F. Tectonic forcing of late Cenozoic climate. *Nature* **359**, 117–122 (1992).
- Galy, V., Beyssac, O., France-Lanord, C. & Eglinton, T. Recycling of graphite during Himalayan erosion: A geological stabilization of carbon in the crust. *Science* **322**, 943–945 (2008).
- Hilton, R. G., Gaillardet, J., Calmels, D. & Birck, J.-L. Geological respiration of a mountain belt revealed by the trace element rhenium. *Earth Planet. Sci. Lett.* **403**, 27–36 (2014).
- Petsch, S. T. in *Treatise on Geochemistry* (eds Holland, H. D. & Turekian, K. K.) 217–238 (Elsevier, 2014).
- Miller, C. A., Peucker-Ehrenbrink, B., Walker, B. D. & Marcantonio, F. Re-assessing the surface cycling of molybdenum and rhenium. *Geochim. Cosmochim. Acta* **75**, 7146–7179 (2011).
- Moon, S., Chamberlain, C. P. & Hilley, G. E. New estimates of silicate weathering rates and their uncertainties in global rivers. *Geochim. Cosmochim. Acta* **134**, 257–274 (2014).
- Derry, L. A. Carbonate weathering, CO₂ redistribution, and Neogene CCD and pCO₂ evolution. *Earth Planet. Sci. Lett.* **597**, 117801 (2022).
- Derry, L. A. & France-Lanord, C. Neogene growth of the sedimentary organic carbon reservoir. *Paleoceanography* **11**, 267–275 (1996).
- Hartmann, J. & Moosdorf, N. The new global lithological map database GLiM: A representation of rock properties at the Earth surface. *Geochem. Geophys. Geosys.* **13**, Q12004 (2012).
- Copard, Y., Amiotte-Suchet, P. & Di-Giovanni, C. Storage and release of fossil organic carbon related to weathering of sedimentary rocks. *Earth Planet. Sci. Lett.* **258**, 345–357 (2007).
- Bolton, E. W., Berner, R. A. & Petsch, S. T. The weathering of sedimentary organic matter as a control on atmospheric O₂: II. Theoretical modeling. *Am. J. Sci.* **306**, 575–615 (2006).
- Larsen, I. J., Montgomery, D. R. & Greenberg, H. M. The contribution of mountains to global denudation. *Geology* **42**, 527–530 (2014).
- Wittmann, H., Oelze, M., Gaillardet, J., Garzanti, E. & von Blanckenburg, F. A global rate of denudation from cosmogenic nuclides in the Earth's largest rivers. *Earth Sci. Rev.* **204**, 103147 (2020).
- Blair, N. E. et al. The persistence of memory: the fate of ancient sedimentary organic carbon in a modern sedimentary system. *Geochim. Cosmochim. Acta* **67**, 63–73 (2003).
- Galy, V., Peucker-Ehrenbrink, B. & Eglinton, T. Global carbon export from the terrestrial biosphere controlled by erosion. *Nature* **521**, 204–207 (2015).
- Grant, K. E., Hilton, R. G. & Galy, V. V. Global patterns of radiocarbon depletion in subsoil linked to rock-derived organic carbon. *Geochim. Persp. Lett.* **25**, 36–40 (2023).
- Garrels, R. M. & Lerman, A. Coupling of the sedimentary sulfur and carbon cycles; an improved model. *Am. J. Sci.* **284**, 989–1007 (1984).
- Kump, L. R. & Arthur, M. A. Interpreting carbon-isotope excursions: carbonates and organic matter. *Chem. Geol.* **161**, 181–198 (1999).
- Regnier, P., Resplandy, L., Najjar, R. G. & Ciais, P. The land-to-ocean loops of the global carbon cycle. *Nature* **603**, 401–410 (2022).
- Dalai, T. K., Singh, S. K., Trivedi, J. R. & Krishnaswami, S. Dissolved rhenium in the Yamuna river system and the Ganga in the Himalaya: role of black shale weathering on the budgets of Re, Os, and U in rivers and CO₂ in the atmosphere. *Geochim. Cosmochim. Acta* **66**, 29–43 (2002).
- Hilton, R. G. et al. Concentration-discharge relationships of dissolved rhenium in alpine catchments reveal its use as a tracer of oxidative weathering. *Water Resour. Res.* **57**, e2021WR029844 (2021).
- Selby, D. & Creaser, R. A. Re–Os geochronology of organic rich sediments: an evaluation of organic matter analysis methods. *Chem. Geol.* **200**, 225–240 (2003).
- Morford, J. L., Martin, W. R. & Carney, C. M. Rhenium geochemical cycling: Insights from continental margins. *Chem. Geol.* **324**, 73–86 (2012).
- Jaffe, L. A., Peucker-Ehrenbrink, B. & Petsch, S. T. Mobility of rhenium, platinum group elements and organic carbon during black shale weathering. *Earth Planet. Sci. Lett.* **198**, 339–353 (2002).
- Colodner, D. et al. The geochemical cycle of rhenium: a reconnaissance. *Earth Planet. Sci. Lett.* **117**, 205–221 (1993).
- Soulet, G. et al. Temperature control on CO₂ emissions from the weathering of sedimentary rocks. *Nat. Geosci.* **14**, 665–671 (2021).
- Roylands, T. et al. Capturing the short-term variability of carbon dioxide emissions from sedimentary rock weathering in a remote mountainous catchment, New Zealand. *Chem. Geol.* **608**, 121024 (2022).
- Tune, A. K., Druhan, J. L., Wang, J., Bennett, P. C. & Rempe, D. M. Carbon dioxide production in bedrock beneath soils substantially contributes to forest carbon cycling. *J. of Geophys. Res. Biogeosci.* **125**, e2020JG005795 (2020).
- Horan, K. et al. Mountain glaciation drives rapid oxidation of rock-bound organic carbon. *Sci. Adv.* **3**, e1701107 (2017).
- Horan, K. et al. Carbon dioxide emissions by rock organic carbon oxidation and the net geochemical carbon budget of the Mackenzie River Basin. *Am. J. Sci.* **319**, 473–499 (2019).
- West, A. J. Thickness of the chemical weathering zone and implications for erosional and climatic drivers of weathering and for carbon-cycle feedbacks. *Geology* **40**, 811–814 (2012).
- Amiotte Suchet, P., Probst, J.-L. & Ludwig, W. Worldwide distribution of continental rock lithology: Implications for the atmospheric/soil CO₂ uptake by continental weathering and alkalinity river transport to the oceans. *Global Biogeochem. Cycles* **17**, 1038 (2003).
- Batjes, N. H. Harmonized soil property values for broad-scale modelling (WISE30sec) with estimates of global soil carbon stocks. *Geoderma* **269**, 61–68 (2016).
- Atwood, T. B., Witt, A., Mayorga, J., Hammill, E. & Sala, E. Global patterns in marine sediment carbon stocks. *Front. Mar. Sci.* **7**, 165 (2020).
- Codilean, A. T. et al. OCTOPUS: an open cosmogenic isotope and luminescence database. *Earth Syst. Sci. Data* **10**, 2123–2139 (2018).
- Amatulli, G., McInerney, D., Sethi, T., Strobl, P. & Domisch, S. Geomorpho90m, empirical evaluation and accuracy assessment of global high-resolution geomorphometric layers. *Sci. Data* **7**, 162 (2020).
- Houlton, B. Z., Morford, S. L. & Dahlgren, R. A. Convergent evidence for widespread rock nitrogen sources in Earth's surface environment. *Science* **360**, 58–62 (2018).
- Hemingway, J. D. et al. Mineral protection regulates long-term global preservation of natural organic carbon. *Nature* **570**, 228–231 (2019).
- Shi, Z. et al. The age distribution of global soil carbon inferred from radiocarbon measurements. *Nat. Geosci.* **13**, 555–559 (2020).
- Luo, Z., Wang, G. & Wang, E. Global subsoil organic carbon turnover times dominantly controlled by soil properties rather than climate. *Nat. Commun.* **10**, 3688 (2019).
- Hartmann, J., Jansen, N., Dürr, H. H., Kempe, S. & Köhler, P. Global CO₂-consumption by chemical weathering: What is the contribution of highly active weathering regions? *Glob. Planet. Change* **69**, 185–194 (2009).
- Walker, J. C. G., Hays, P. B. & Kasting, J. F. A negative feedback mechanism for the long-term stabilization of Earth's surface temperature. *J. Geophys. Res. Oceans* **86**, 9776–9782 (1981).
- Plank, T. & Manning, C. E. Subducting carbon. *Nature* **574**, 343–352 (2019).
- Smith, R. W., Bianchi, T. S., Allison, M., Savage, C. & Galy, V. High rates of organic carbon burial in fjord sediments globally. *Nat. Geosci.* **8**, 450–453 (2015).
- Evans, M. J., Derry, L. A. & France-Lanord, C. Degassing of metamorphic carbon dioxide from the Nepal Himalaya. *Geochim. Geophys. Res.* **9**, 4 (2008).
- Märki, L. et al. An unshakable carbon budget for the Himalaya. *Nat. Geosci.* **14**, 745–750 (2021).

Publisher's note Springer Nature remains neutral with regard to jurisdictional claims in published maps and institutional affiliations.



Open Access This article is licensed under a Creative Commons Attribution 4.0 International License, which permits use, sharing, adaptation, distribution and reproduction in any medium or format, as long as you give appropriate credit to the original author(s) and the source, provide a link to the Creative Commons licence, and indicate if changes were made. The images or other third party material in this article are included in the article's Creative Commons licence, unless indicated otherwise in a credit line to the material. If material is not included in the article's Creative Commons licence and your intended use is not permitted by statutory regulation or exceeds the permitted use, you will need to obtain permission directly from the copyright holder. To view a copy of this licence, visit <http://creativecommons.org/licenses/by/4.0/>.

© The Author(s) 2023

Methods

The workflow of materials and methods (Extended Data Fig. 1) starts with the compilation and derivation of rhenium-concentration-based OC_{petro} oxidation flux estimates, discussed just below. Then we detail the 'Global spatial OC_{petro} oxidation model' and its application of sub-models for OC_{petro} stocks and denudation, and the Monte Carlo routines used in the model's approach. Finally, we discuss the 'Limitations and uncertainties' involved in our methods and calculations.

Rhenium-based river catchment estimates of OC_{petro} oxidation

From a series of dissolved rhenium measurements (typically completed by ICP-MS), the dissolved Re flux J_{Re} (t yr^{-1}) can be used to estimate OC_{petro} oxidation flux, $J_{OC_{\text{petro-ox}}}$ (tC yr^{-1}) using:

$$J_{OC_{\text{petro-ox}}} = J_{\text{Re}} \times \left(\frac{[OC_{\text{petro}}]}{[Re]} \right)_i \times f_c \quad (2)$$

where f_c is the fraction of dissolved Re derived from OC_{petro} oxidation³⁴ and $([OC_{\text{petro}}]/[Re])_i$ is the organic carbon to rhenium concentration ratio (g g^{-1}) in rocks of type i undergoing weathering. In some catchments where it may be important, an additional term, not shown in equation (2), has been applied to correct for the presence of graphite, which may not undergo alteration during weathering³³.

Compiled published measurements. In this study we compile estimates of OC_{petro} oxidation using the dissolved Re proxy from published literature (Supplementary Table 1). These include the Yamuna River, India²⁴; ten Taiwanese rivers⁷; four rivers from the western Southern Alps³³; four rivers from the Mackenzie Basin, Canada^{3,34}; and six rivers draining the Peruvian Andes³¹. Two Swiss catchments²⁵ are not included because of their very small catchment area compared to the geospatial scales over which we complete the upscaling.

For some of these case studies, dissolved rhenium flux has been estimated from repeated sampling and discharge records³⁴, while earlier studies all include single snapshot samples^{7,24}, and all include measurements of the local sedimentary rock composition. Most of these compiled studies have used dissolved ion ratios to estimate the source of dissolved Re, akin to f_c (equation (2)), apart from the Taiwan dataset⁷. While uncertainties on the OC_{petro} oxidation yields appear relatively large (Supplementary Table 1), it is important to note that the measured range in yields is much larger than the uncertainties.

New estimates of OC_{petro} oxidation. To expand the 25 estimates of OC_{petro} oxidation from river catchments described previously, we build on a previous study of dissolved Re fluxes in large rivers that reports dissolved Re concentrations and fluxes for major basins around the world⁹. We use these measurements and combine them with estimates of f_c and $([OC_{\text{petro}}]/[Re])_i$, discussed in the following sections, to calculate OC_{petro} oxidation yields with associated uncertainties using published approaches^{25,34}.

In locations with substantial local sources of fossil fuel combustion (for example, coal-fired power plants or steel works), rainwater can contain concentrations of Re that approach those of river water^{8,52}, whereas locations that have minimal impacts from local pollution sources have Re concentrations in rainwater that are below detection^{25,33}. In the large river dataset⁹, some large rivers are noted to have markedly increased Re concentrations and fluxes; the conclusion is that this was due to anthropogenic Re inputs. In a first-order catchment of the Mississippi Basin, this has been confirmed by a detailed Re mass balance⁵². A study of Re across Indian catchments suggests that while Re in Himalayan catchments and the mainstem Ganges and Brahmaputra behave conservatively, peninsular lower relief catchments with denser populations and industrial activity suggest anthropogenic inputs⁵³. For this study's purpose, to quantify weathering reactions, we only use

Himalayan rivers and the mainstem Ganges and Brahmaputra in India, and we have further excluded Re data from the Danube, Mississippi and Yangtze rivers from our analysis. Our addition of catchment Re data to the Miller dataset includes a large contribution of small upland catchments with higher average erosion rates, where the authors of these studies selected sites with minimal human disturbance (Supplementary Table 1). We further consider the role of anthropogenic Re in our model results in the 'Limitations and uncertainties' section.

Estimation of Re source and f_c . To estimate the fraction f_c of dissolved Re sourced from OC_{petro} for the rivers in the Re flux dataset⁹, we follow a previously used forward model mixing approach^{25,34}:

$$Re_{OC} = Re_{\text{tot}} \times f_c = Re_{\text{tot}} - Re_{\text{sulf}} - Re_{\text{sil}} \quad (3)$$

where Re_{OC} is the rhenium concentration of OC_{petro} -derived Re in the dissolved load, Re_{tot} is the measured Re concentration, Re_{sulf} and Re_{sil} are the concentrations derived from weathering of sulfide and silicate minerals, respectively. These unknowns can be quantified as:

$$Re_{\text{sulf}} = [SO_4] \times \left(\frac{[Re]}{[SO_4]} \right)_{\text{sulf}} \quad (4)$$

$$Re_{\text{sil}} = [Na] \times \left(\frac{[Re]}{[Na]} \right)_{\text{sil}} \quad (5)$$

where the element ratios of the end members for silicate, $([Re]/[Na])_{\text{sil}}$ and sulfide, $([Re]/[SO_4])_{\text{sulf}}$ are defined, and with the assumption that the dissolved sulfate (SO_4) and sodium (Na) respectively derive only from sulfide oxidation and silicate weathering and are conservative. This returns an upper bound on the Re_{sulf} and Re_{sil} components (Supplementary Table 2). Following recent work³⁴, we use a range of values for each, where $([Re]/[SO_4])_{\text{sulf}}$ ranges from 0.2×10^{-3} to $4 \times 10^{-3} \text{ pmol } \mu\text{mol}^{-1}$ (ref. 23) and $([Re]/[Na])_{\text{sil}}$ ranges from 0.4×10^{-3} to $2 \times 10^{-3} \text{ pmol } \mu\text{mol}^{-1}$. Here, we correct Na^+ concentrations for atmospheric-derived Na, $[Na^+]^*$, where $[Na^+]^* = [Na^+] - [Cl^-] \times 0.8$, assuming all Cl^- derives from precipitation, which has a molar $[Na^+]/[Cl^-]$ ratio of 0.8. We similarly correct for atmospheric SO_4 inputs.

Constraints on $([OC_{\text{petro}}]/[Re])_i$. A recent compilation⁵⁴ provides measurements of $([OC_{\text{petro}}]/[Re])_i$ from rock samples of different ages around the world. However, most of these measurements were made on black shales with OC_{petro} contents greater than 1%, which occur on only 0.3% of the Earth surface (Extended Data Fig. 5). Riverbed material sediments from erosive catchments provide an alternative way to capture landscape-scale average rock composition, albeit with some potential for weathering to alter the primary signal. Here we compile measurements of $[OC_{\text{petro}}]/[Re]$ on bed materials from rivers around the world (Supplementary Table 3 and Extended Data Fig. 2) and supplement this dataset with additional samples from mudrocks of the Eastern Cape, New Zealand, and the Peruvian Andes measured using methods described previously²⁵. We find that regions with lower OC_{petro} concentrations that are more typical of sedimentary rocks at the continental surface—units including fine-grained sedimentary rocks that make up more than 35% of Earth surface (Extended Data Fig. 5)—have lower and more consistent ratios of OC and Re in their rocks. The samples from the Peel River in the Mackenzie River basin³⁴ overlap the lower end of the published black shale values. Since this is the catchment with the highest proportion of black shales in our Re dataset, these samples allow us to capture the imprint of this important marginal lithology at the landscape scale.

The bedrock composition in the catchments of rivers studied in the Re flux dataset⁹ is not reported. However, we note the good geographic coverage and number of samples that we have from riverbed materials

from erosive settings around the world. These provide constraint on the initial OC to rhenium ratio in the rocks. To conservatively quantify uncertainty in the range of OC_{petro} oxidation rates from dissolved-Re data, we perform a Monte Carlo simulation in which we uniformly sample the entire range of measured $[OC_{\text{petro}}]/[Re]$ values, from low values indicative of carbon-poor and/or metamorphic rocks $2.5 \times 10^{-8} \text{ g g}^{-1}$ (ref. 33) towards $1.26 \times 10^{-6} \text{ g g}^{-1}$ (ref. 34) in catchments with higher OC in rocks (Supplementary Table 3 and Extended Data Fig. 3).

OC_{petro} oxidation yields and uncertainties. Equation (2) is used for each basin in the Re flux dataset⁹. Uncertainties in f_c derive from the range of values used in the sulfide and silicate end member compositions (equations (4) and (5)). For $[OC_{\text{petro}}]/[Re]$, we use the range of values discussed in the just-previous section on constraints (Extended Data Fig. 3). A Monte Carlo uncertainty propagation is used on these variables, with 10,000 randomly selected combinations of input values (with uniform sampling) are used to estimate $J_{OC_{\text{petro-ox}}}$ for each basin. The median value of the Monte Carlo simulation and the interquartile range are reported (Supplementary Table 1).

Geospatial catchment boundaries. To derive the catchment outlines and areas corresponding to the Re-proxy samples in our compiled dataset, we used the HYDROSHEDS flow direction grid at 3 arc-second resolution⁵⁵ and ArcGIS Pro⁵⁶. Catchments outside the latitudinal cover of HYDROSHEDS were derived from the HYDRO1K flow direction grid⁵⁷ and catchments in Iceland were derived from ALOS AW3D using TauDEM functionality in OpenTopography⁵⁸. While most published sample coordinates (Supplementary Table 1) give the correct location on the cited drainage systems, in a handful of cases, coordinates had to be amended by up to a few kilometres, which may reflect errors in transcribing (for example, Kikori and Purari⁹). Final quality control included a comparison of the extracted drainage basin areas and those published, with good agreement overall (less than 2% residual). However, some drainage areas cited in the Re flux dataset⁹ refer to the river mouth, rather than the river catchment upstream of the Re sample location. In these cases, we use the Re sample location and its upstream catchment. Finalized coordinates of Re samples determined for each drainage system, with the corresponding upstream drainage area, are given in Supplementary Table 1. Spatial files of upstream drainage boundaries and Re sample locations are available on Zenodo (available from <https://doi.org/10.5281/zenodo.8144244>). To convert dissolved Re concentrations into Re fluxes, average annual water discharge was calculated using published numbers at gauges (Supplementary Table 1) and scaled to the upstream drainage area of Re sample locations.

In addition to spatial catchment boundaries for the Re proxy dataset, we compare our spatial model output to published estimates of silicate weathering¹⁰ that use the GRDC dataset in *Major River Basins of the World*⁵⁹. Drainage areas used by ref. 10 have slight discrepancies with those found in the GRDC dataset. We account for these in our analysis of major river basin net weathering flux (Supplementary Table 4).

Global spatial OC_{petro} oxidation model

In the following three sections, we provide additional rationale and details of the modelling approaches. The model procedures apply two spatial probabilistic subroutines; one deals with OC_{petro} stocks in surface rocks and the other with spatially defined denudation rates. These are combined in a Monte Carlo framework alongside the Re-proxy river catchment data to optimize the model and then extrapolate OC_{petro} oxidation rates (Extended Data Fig. 1). Model simulations were implemented at 1-km grid scale (Mollweide projection, WGS84 datum) in the Python programming language⁶⁰.

OC_{petro} stocks. Rock samples from the USGS Rock Geochemical Database, sorted into lithological categories (Supplementary Table 5), were mapped onto units of the highest-resolution global lithological maps

currently available¹³. Extended Data Fig. 4 shows the OC_{petro} concentration of key lithologies in the USGS Rock Geochemical Database. Weight percentage values from the USGS Rock Geochemical Database were converted to OC_{petro} stock using rock densities (Supplementary Table 5). In our Monte Carlo framework, OC_{petro} stocks at each grid cell were sampled independently using the empirical distributions of rock OC_{petro} content derived from both the USGS database (Extended Data Fig. 4) and our unit classification (Supplementary Table 5). In our lithology model, complex mapped units present in GLiM consist of a combination of carbonates and silicates of various grain sizes (Extended Data Fig. 5 and Supplementary Table 5). To calculate the OC_{petro} reservoir among these units, we derive the fractional abundance of lithology types (F_n) from continental-scale literature estimates³⁶:

$$[OC_{\text{petro}}]_{\text{rock}} = F_1([OC_{\text{petro}}]_{\text{lithology},1}) + F_2([OC_{\text{petro}}]_{\text{lithology},2}) + \dots + F_n([OC_{\text{petro}}]_{\text{lithology},n}) \quad (6)$$

$$F_1 + F_2 + \dots + F_n = 1 \quad (7)$$

Denudation model. The denudation model is parametrized using a regression approach, similar to techniques applied elsewhere^{16,41}. We regressed a compilation of long-term catchment-scale ¹⁰Be denudation estimates³⁹ against mean local slope generated from the Geomorpho90m dataset⁴⁰. Mean local slope was calculated using the focal statistics tool in ArcGIS Pro⁵⁶ and the Geomorpho90m slope dataset with a 5-km moving radius. Slope values were then matched to ¹⁰Be denudation estimates at a single cell based on the reported longitude and latitude. A quantile regression approach^{41,61,62}, allows us to mitigate over- and underestimations inherent in using a mean model fit to the global land surface¹⁶ (Extended Data Fig. 6). For each unique slope value in the global raster, denudation quantiles were used to construct a cumulative distribution function which could be sampled in each Monte Carlo run (compare ref. 41).

We account for differential erodibilities of sedimentary, crystalline metamorphic and igneous rock types by running regressions between slope values and ¹⁰Be values for each rock type (Extended Data Fig. 6). Thus, only ¹⁰Be values from catchments dominated (more than 80%) by one rock type are used in this regression. This accounting of erodibilities is important, as OC-rich shales are weaker and more erodible than OC-poor strong igneous rocks. Residuals between the CRN denudation dataset and the modelled denudation do not change when differential rock erodibility is considered. However, when combined with our OC_{petro} stock model, the rock erodibility-corrected OC supply rate model results in 20% higher rates. We also consider the grid-scale bias considered by previous workers^{16,41}: as DEM resolution decreases, slope—as the spatial derivative of elevation—decreases, resulting in an artificial flattening effect¹⁶. As our Monte Carlo framework is computationally intensive, using a 90-m-resolution global raster input would not be feasible. However, we use a 90-m-resolution slope dataset to run regression curves as shown in Extended Data Fig. 6, after which we output a 90-m-resolution raster dataset of estimated denudation rates using the median regression curve. By resampling the raster dataset of estimated denudation rates to 1-km resolution after conversion from slope values, we avoid the bias that can lead to an underestimation of denudation by the flattening effect. In our Monte Carlo framework, the quantile regression curves for each raster value can then be sampled to draw a representative denudation value out of the empirical distribution of denudation rates.

Model calibration. The global model is calibrated by minimizing the residual with the Re-proxy-based estimates of OC_{petro} oxidation (tC yr^{-1}) from 59 globally distributed river basins (Supplementary Table 1). Model selection was performed by running a Monte Carlo simulation

(10,000 runs), using the variable OC_{petro} stock and denudation models described above, to find the output which minimizes total residuals across all 59 calibration basins simultaneously, such that the sum of all basin residuals was less than 1%. These simulations were run on the University of Oxford's Advanced Research Computing (ARC) facility, taking about 24 core hours per simulation. The residuals of individual basins can be quite large for the biggest catchments (for example, the Amazon basin), but the relative residual, especially for the larger basins, falls within the uncertainty of model outputs, while accurately predicting the total OC_{petro} oxidation flux globally (Extended Data Fig. 7). We note that, overall, in basins with moderate OC_{petro} oxidation fluxes, the model may return conservative estimates. However, because this model has the advantage of being globally and spatially explicit, regional over- and underestimation of OC_{petro} oxidation found mostly at a local scale (less than 10,000 km²) tend to trade off while we are able to capture larger regional differences due to tectonics and geological setting (Fig. 1d).

Limitations and uncertainties

There is a temporal mismatch between the CRN denudation data that inform our probabilistic denudation model, and our Re-proxy calibration data. The Re-proxy-based OC_{petro} oxidation fluxes used to calibrate our spatial extrapolation model capture fluxes from global rivers within the past decade or less. The CRN technique integrates denudation fluxes that span a millennium or more. Anthropogenic land-use change has doubled erosion and weathering since the early 1900s (ref. 63); hence, our global scale estimates of OC_{petro} oxidation rates reflect the combined influence of natural and anthropogenic activities on global weathering rates, which cannot be deconvolved in this present study.

Results of model versus Re-predicted OC_{petro} oxidation fluxes help us assess the potential for anthropogenic Re input to impact our estimates (Extended Data Fig. 7). We have considered anthropogenic Re inputs by removing three large river basins from a previous compilation⁹ and by adding carefully selected river catchment sites to our Re dataset (see the Methods section headed 'Rhenium-based river catchment estimates of OC_{petro} oxidation'). In addition, our conversion of Re fluxes to OC_{petro} oxidation is conservative because we uniformly sample the range of Re/OC ratios starting at the lowest measured Re/OC ratio (see the Methods section headed 'Constraints on ($OC_{\text{petro}}/[Re]$)'). This leads to error bars within our estimates that are conservatively large. Most notably, the model outputs of OC_{petro} oxidation versus the Re-estimated fluxes for each basin (Extended Data Fig. 7) show a tendency for the model to underpredict smaller catchments more than larger catchments. Our confidence in the weathering signal from Re in the small upland catchments is highest, and the upland, high-erosion-rate regions that these catchments sample contribute a dominant proportion of the global OC_{petro} flux in our model. While we cannot completely deconvolve the effect of anthropogenic Re in our constraints, we have confidence that the effect is unlikely to result in a significant overprediction of global OC_{petro} flux estimates.

The global extrapolation of OC_{petro} oxidation proxy data attempts to account for the dataset's underlying heterogeneities in denudation and OC_{petro} stocks. However, it does not consider variability in temperature or precipitation which may control weathering—as seen in small-scale field measurements of OC_{petro} oxidation at sites of high denudation^{30,31}. This is primarily due to the size of the Re-proxy catchment database, its spatial coverage and uncertainties inherent in any proxy approach. While the Re-proxy dataset is latitudinally variable (Fig. 1a) the model misfit minimization procedure shows the first-order controls on flux by OC_{petro} stock and denudation (Extended Data Fig. 7), meaning that any climatic controls on weathering could be not resolved at the global scale. We note that any bias introduced by extrapolating the global Re-proxy data without including climatic spatial controls on weathering intensity is likely to be minimal, because the underlying dataset spans from the tropics to Arctic locations.

Previous work has suggested that OC_{petro} oxidation and cycling of other OC pools can take place during floodplain transport in large fluvial systems^{64,65}. While the Re-proxy dataset includes large basins with extensive floodplain areas (Fig. 1a), our model–data misfit approach may attribute the downstream fluxes to any higher denudation parts of the catchment. When the model is then upscaled, in lowland floodplain areas where fluvial processing and recycling of sediment⁶⁵ can allow biogeochemical reactions to continue⁶⁵, we may predict conservative OC_{petro} oxidation rates. At present, we lack empirical data to partition weathering between mountain and floodplain sections³. An alternative way to view this is that the removal of alluvial domains from contributing to denudation (since these are depositional) holds minimal control on the overall estimate (less than 1%). This result comes from a comparison of model outputs under two parametrization schemes: one where denudation occurs over all ice-free lands versus one where denudation only occurs in ice-free non-alluvial landscapes. Overall, the model's largest contributor to uncertainty is in the conversion of dissolved Re fluxes to OC_{petro} oxidation estimates, which are extrapolated in our spatial model. This conversion depends on $[OC_{\text{petro}}]/[Re]$ ratios which introduce most of the uncertainty in the resulting OC_{petro} oxidation rates (see the Methods section 'OC_{petro} oxidation yields and uncertainties') and therefore in the model's global output. More constraints on the relative 'grey shale' versus 'black shale' contribution to catchment Re fluxes could help tighten uncertainty in $[OC_{\text{petro}}]/[Re]$ ratios (see ref. 66 for a discussion).

Finally, our model includes implicit assumptions and features of the datasets which must be acknowledged. First, the model assumes a steady state, which might not accurately describe OC_{petro} oxidation in regions responding to changes in uplift, deglaciation or human activities, which may not yet have reached steady-state conditions.

Second, most catchment-scale CRN denudation data used in our model derive from lithologies that are quartz-rich and coarse-grained. These typically have lower erodibilities, potentially leading to an underestimation of denudation rates of softer shales which contain the majority of OC_{petro} stocks.

Data availability

All dissolved rhenium sample data are available in Supplementary Tables 1–5, in addition to which geospatial data, including those for Fig. 1, are deposited in a Zenodo repository (<https://doi.org/10.5281/zenodo.8144244>). Source data are provided with this paper.

Code availability

The spatial OC_{petro} oxidation model contains two spatial probabilistic subroutines of (1) OC_{petro} stocks in surface rocks and (2) spatially defined denudation rates. These are combined in a Monte Carlo framework alongside the Re-proxy river catchment data to optimize the model and then extrapolate OC_{petro} oxidation rates (Extended Data Fig. 1). Model simulations were implemented at 1-km grid scale (Mollweide projection, WGS84 datum) in the Python programming language. Rand Python code, their environments and the necessary data files to run these are all deposited in a Zenodo repository (<https://doi.org/10.5281/zenodo.8144244>) and additionally code is available from GitHub: https://github.com/jessezondervan/Global_OCpetro_Oxidation.

- Dellinger, M. et al. High rates of rock organic carbon oxidation sustained as Andean sediment transits the Amazon foreland-floodplain *Proc. Natl. Acad. Sci. USA* **120**, e2306343120 (2023). <https://doi.org/10.1073/pnas.2306343120>.
- Ogrić, M. et al. Low rates of rock organic carbon oxidation and anthropogenic cycling of rhenium in a slowly denuding landscape. *Earth Surf. Process. Landf.* **48**, 1202–1218 (2023).
- Rahaman, W., Singh, S. K. & Shukla, A. D. Rhenium in Indian rivers: sources, fluxes, and contribution to oceanic budget. *Geochem. Geophys. Geosystems* **13**, Q08019 (2012).
- Sheen, A. I. et al. A model for the oceanic mass balance of rhenium and implications for the extent of Proterozoic ocean anoxia. *Geochim. Cosmochim. Acta* **227**, 75–95 (2018).

55. Lehner, B., Verdin, K. & Jarvis, A. New global hydrography derived from spaceborne elevation data. *Eos T. Am. Geophys. Un.* **89**, 93–94 (2008).
56. ArcGIS Pro, Release 2.8 (Environmental Systems Research Institute, 2021).
57. Earth Resources Observation and Science (EROS) Center. USGS EROS Archive - Digital Elevation - HYDRO1K. U.S. Geological Survey <https://doi.org/10.5066/F77P8WNO> (2000).
58. Japan Aerospace Exploration Agency. ALOS World 3D - 30 m. V3.2. *OpenTopography* <https://doi.org/10.5069/G94M92HB> (2021).
59. GRDC. Major river basins of the world. *Global Runoff Data Centre, GRDC*, 2nd, rev. ext. ed. (Federal Institute of Hydrology (BfG), 2020); https://www.bafg.de/GRDC/EN/02_srvcs/22_gslrs/221_MRB/riverbasins_node.html#doc2731742bodyText8.
60. *Python Language Reference* version 3.9 <https://docs.python.org/3.9/reference/index.html> (Python Software Foundation, 2020).
61. Koenker, R. quantreg: quantile regression. R package version 5.94 <https://CRAN.R-project.org/package=quantreg> (2022).
62. R Core Team. *R: A Language and Environment for Statistical Computing* (R Foundation for Statistical Computing, 2021) <https://www.R-project.org/>.
63. Syvitski, J. et al. Earth's sediment cycle during the Anthropocene. *Nat. Rev. Earth & Environ.* **3**, 179–196 (2022).
64. Bouchez, J. et al. Oxidation of petrogenic organic carbon in the Amazon floodplain as a source of atmospheric CO₂. *Geology* **38**, 255–258 (2010).
65. Repasch, M. et al. Fluvial organic carbon cycling regulated by sediment transit time and mineral protection. *Nat. Geosci.* **14**, 842–848 (2021).
66. Charbonnier, Q., Bouchez, J., Gaillardet, J., Calmels, D. & Dellinger, M. The influence of black shale weathering on riverine barium isotopes. *Chem. Geol.* **594**, 120741 (2022).
67. Crawford, I. et al. in *Targeted Geoscience Initiative: 2018 Report of Activities* (ed. Rogers, N.) 139–161 (Geological Survey of Canada, 2019); <https://doi.org/10.4095/313647>.
68. Peucker-Ehrenbrink, B. Land2Sea database of river drainage basin sizes, annual water discharges, and suspended sediment fluxes. *Geochem. Geophys. Geosystems* **10**, Q06014 (2009).

Acknowledgements We would like to acknowledge the use of the University of Oxford Advanced Research Computing (ARC) facility in carrying out this work (<https://doi.org/10.5281/zenodo.22558>). In addition, this work is based on digital elevation products and high-performance topographic analysis services provided by the OpenTopography Facility with support from the National Science Foundation under NSF Award Numbers 1948997, 1948994 and 1948857. This study was supported by the European Research Council Starting Grant ROC-CO2 678779 (R.G.H.).

Author contributions J.R.Z. and R.G.H. conceptualized the study. J.R.Z., R.G.H. and F.J.C. developed the methodologies. J.R.Z. and R.G.H. conducted the investigation. R.G.H., M.D., T.R. and M.O. acquired the resources. Data visualization was done by J.R.Z. and R.G.H., while J.R.Z., R.G.H. and M.D. curated the data. R.G.H. acquired the funding. J.R.Z. and R.G.H. wrote the original draft of the paper. The paper was reviewed and edited by all the authors.

Competing interests The authors declare no competing interests.

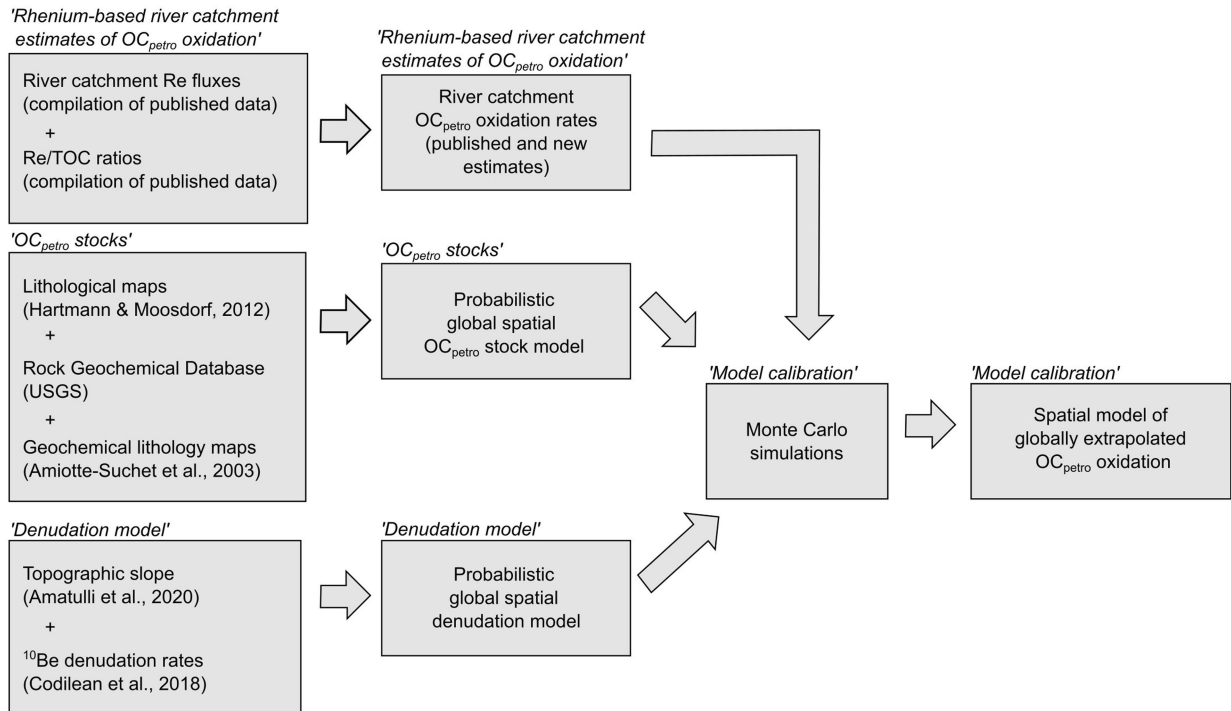
Additional information

Supplementary information The online version contains supplementary material available at <https://doi.org/10.1038/s41586-023-06581-9>.

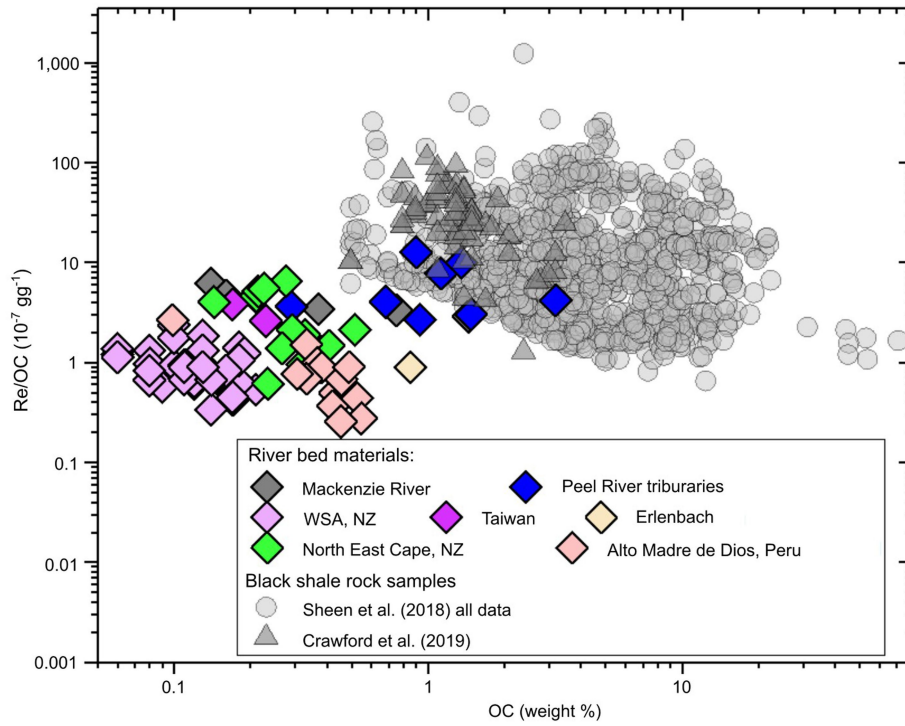
Correspondence and requests for materials should be addressed to Jesse R. Zondervan or Robert G. Hilton.

Peer review information *Nature* thanks Louis Derry and Bernhard Peucker-Ehrenbrink for their contribution to the peer review of this work. Peer reviewer reports are available.

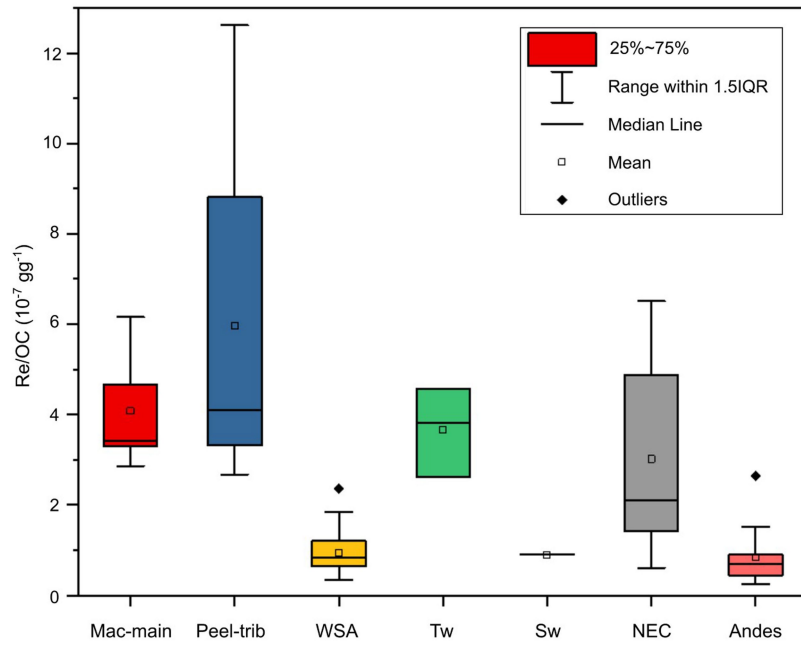
Reprints and permissions information is available at <http://www.nature.com/reprints>.



Extended Data Fig. 1 | Flow chart of data, subroutines and outcomes and the relevant Methods sections. Probabilistic geospatial models of OC_{petro} stocks and denudation are used to extrapolate a global compilation of river catchment OC_{petro} oxidation rates across the Earth's surface.

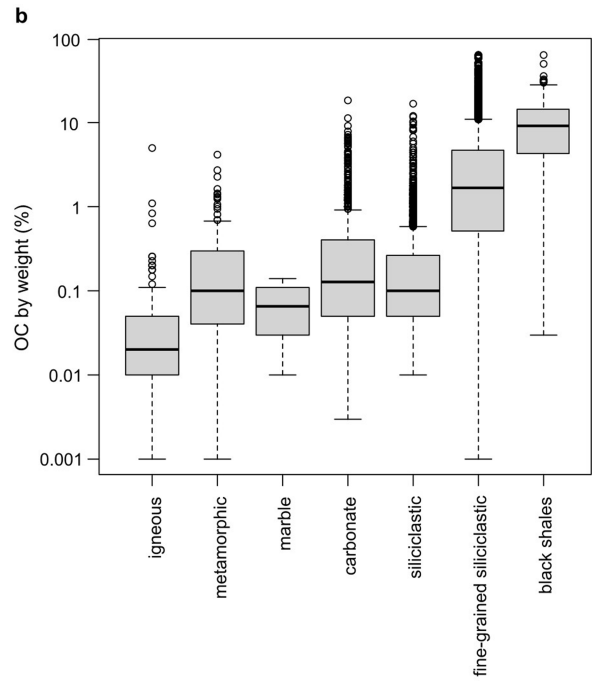
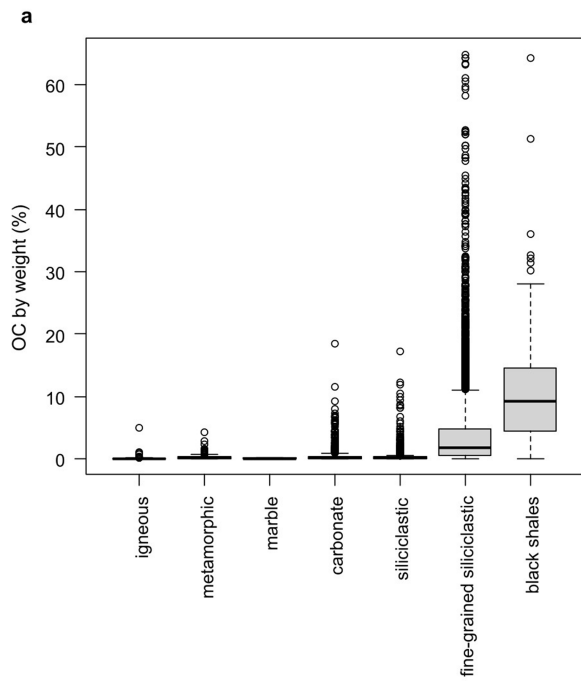


Extended Data Fig. 2 | Rhenium (Re) to organic carbon (OC) concentration ratio (10⁻⁷ gg⁻¹) in published black shales^{54,67} alongside those measured in riverbed materials (Supplementary Table 3). Peel riverbed materials capture the input of OC from black shale lithologies, which in other basins are much less common.



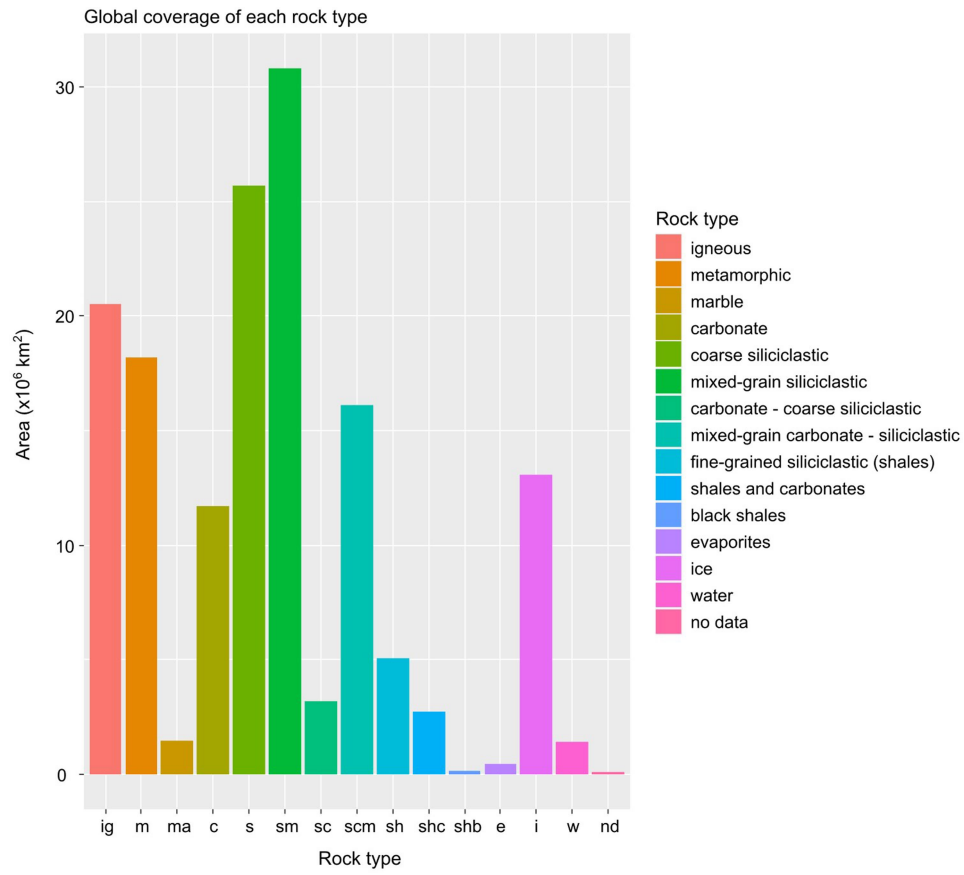
Extended Data Fig. 3 | Rhenium (Re) to organic carbon (OC) concentration ratio (10^{-7} g g^{-1}) of riverbed materials, organized by sample location (Supplementary Table 3). Conservatively, the Monte Carlo analysis of OC_{petro} oxidation rates from the dissolved rhenium proxy uniformly samples the

complete measured range of Re/OC values presented here. Sample groups are as follows: Mac-main = Mackenzie River; Peel-trib = Peel river tributaries; WSA = Western Southern Alps, New Zealand; Tw = Taiwan rivers; Sw = Swiss rivers; NEC = North East Cape, New Zealand; Andes = Madre de Dios catchment.

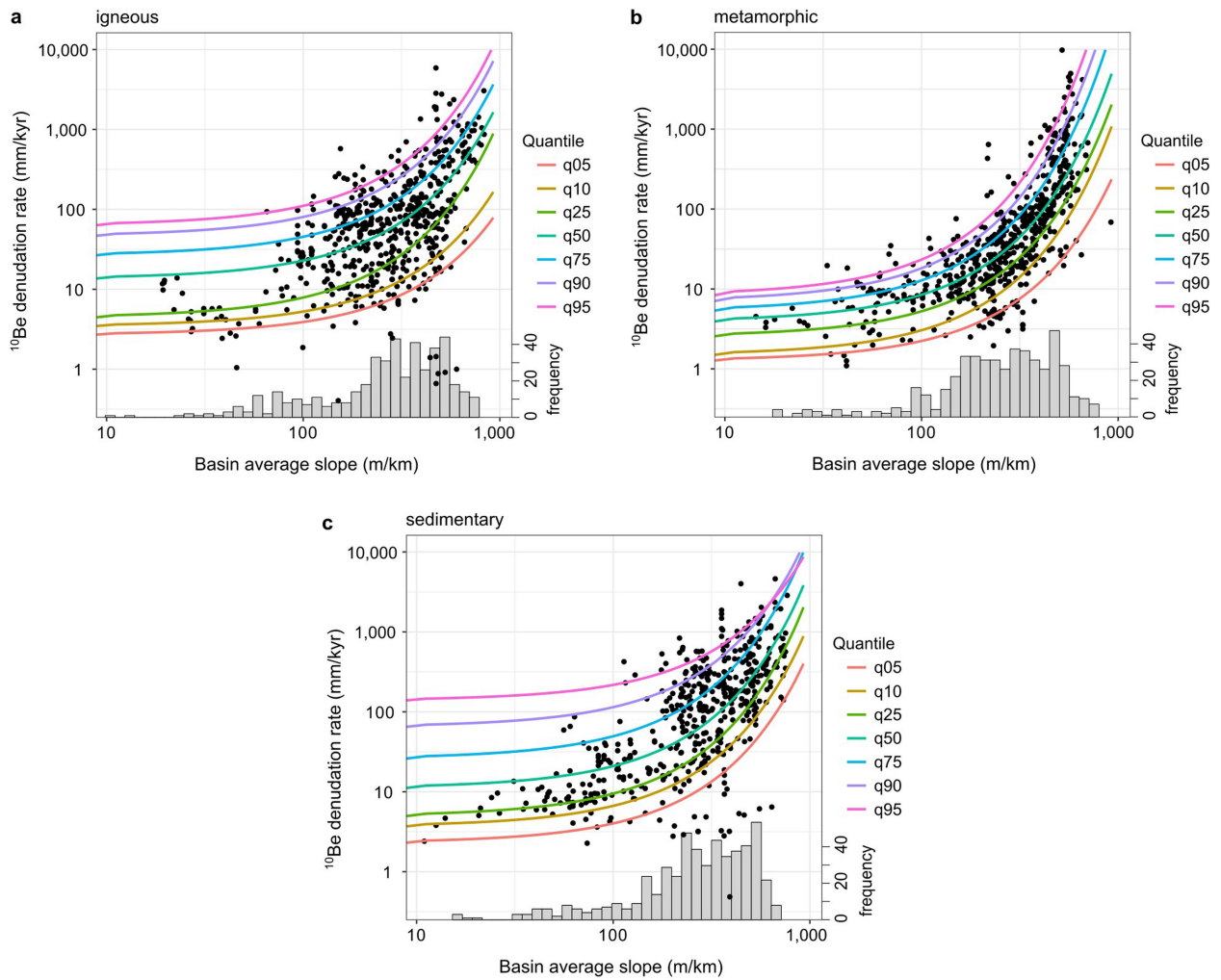


Extended Data Fig. 4 | Organic carbon concentrations (OC in weight %) of lithological types in the USGS Rock Geochemical Database (a) and the same figure in log scale (b). Black lines show median values, boxes show the

interquartile range (IQR), whiskers show $IQR + 1.5 \times IQR$, and outliers are shown as open symbols (although still included in the analysis).

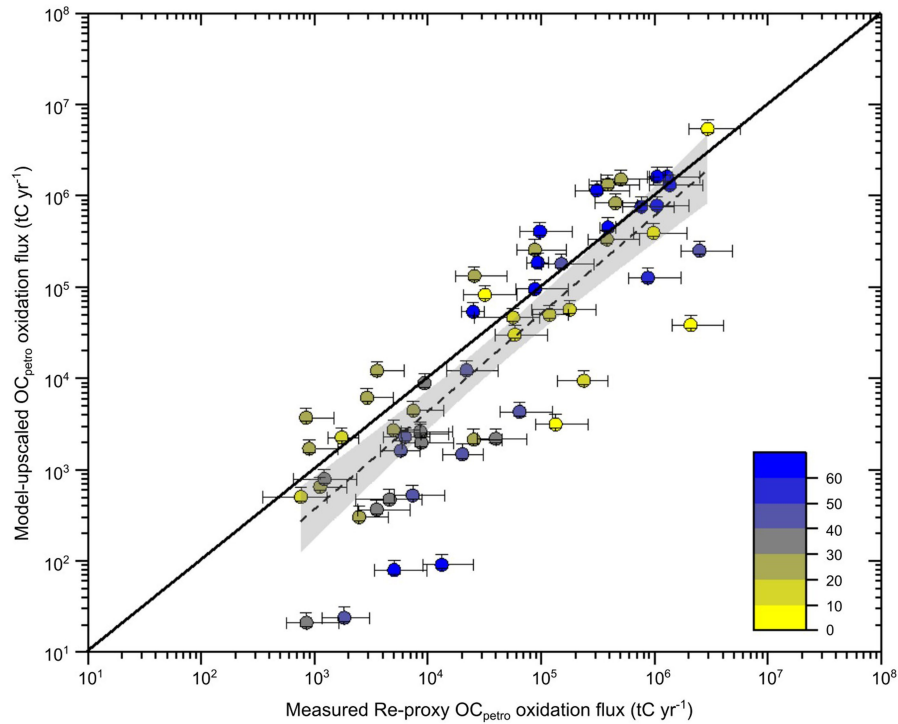


Extended Data Fig. 5 | Total continental area (m²) of each mapped units from the GLiM model¹³. Mapped units include mixed units of siliciclastic lithologies with various grain-sizes (fine and coarse) and mixes of carbonate and siliciclastic lithologies¹³.



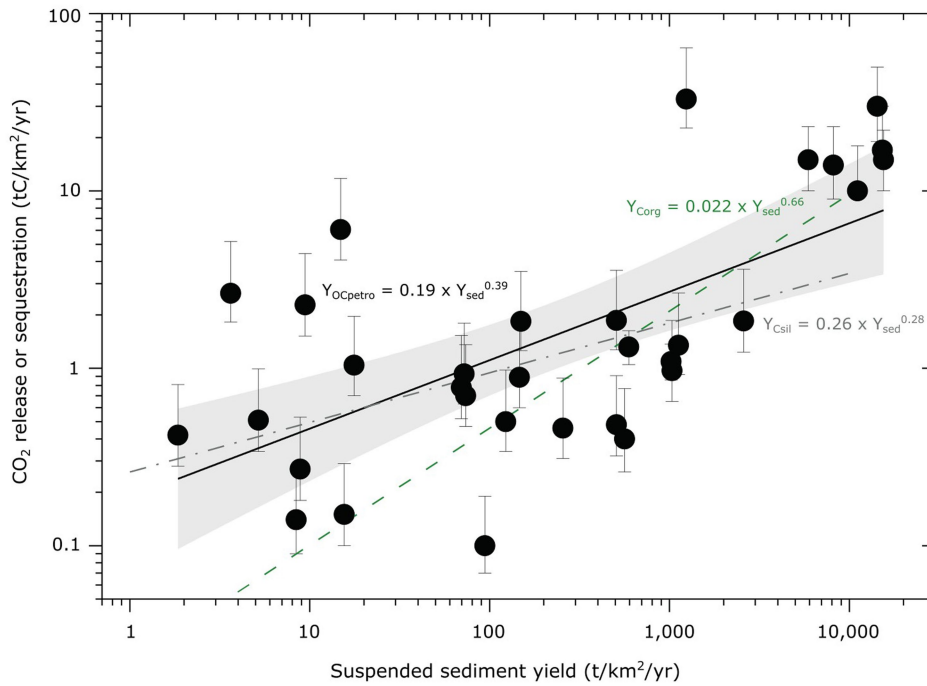
Extended Data Fig. 6 | Cosmogenic isotope-derived denudation rates (^{10}Be erosion rate mm/kyr) from the OCTOPUS dataset³⁹ analysed here. Sites are grouped by dominant lithology and the denudation rate as a function of basin average slope (m/km) returned by quantile regression for (a) igneous,

(b) metamorphic, and (c) sedimentary dominated catchments. The quantiles corresponding to each grid cell slope value constitute cumulative density functions (CDFs) which can be sampled in each Monte Carlo simulation that quantifies global oxidative weathering rates (Extended Data Fig. 1).



Extended Data Fig. 7 | Rock organic carbon (OC_{petro}) oxidation rate (tC yr⁻¹) from the Re-proxy versus the model upscaled output for the global set of catchments used in this study (Supplementary Table 1). Catchments are coloured by the latitude of the sampling point (0° to 80° N and S). Error bars represent uncertainty in Re-proxy values for OC_{petro} oxidation (see Methods

sections headed 'Rhenium-based river catchment estimates of OC_{petro} oxidation' & 'OC_{petro} oxidation yields and uncertainties') and the resultant uncertainty in extrapolation model outputs. The dashed line and grey shading shows fit to the data (95% confidence intervals) and the solid black line shows 1:1 line.



Extended Data Fig. 8 | CO₂ release through OC_{petro} oxidation (black dots, this study; Y_{OCpetro}, black line) is more sensitive to sediment yield than CO₂ sequestration through silicate weathering (Y_{CSil}, grey dotted-dashed line)⁴, whilst terrestrial biospheric OC burial (Y_{Corg}, green dashed line)¹⁹ could be even more sensitive. CO₂ sequestration trendlines are from Galy et al.¹⁹ The black dots show CO₂ release through OC_{petro} oxidation for all the Re sample catchments which have suspended sediment yield data available from the

Land2Sea database⁶⁸ (Supplementary Table 1) to allow comparison with the previous assessment of silicate weathering vs biospheric OC burial¹⁹. The exponent for Y_{OCpetro} is 0.39 ± 0.08 with $r^2 = 0.43$, reflecting the scatter in data owing to the spatial dependence of OC_{petro} oxidation on rock OC content and denudation rates (Fig. 2). Therefore, comparisons based on the global trends in this plot, without considering their spatial context (see Fig. 2 for spatially explicit comparisons), should be done with care considering the low certainty.